

See discussions, stats, and author profiles for this publication at: <https://www.researchgate.net/publication/263581538>

# Facile Molecular Approach to Transparent Thin-Film Field-Effect Transistors with High-Performance Using New Homo- and Heteroleptic Indium(III)–Tin(II) Single-Source Precursors

ARTICLE *in* CHEMISTRY OF MATERIALS · MAY 2012

Impact Factor: 8.35 · DOI: 10.1021/cm300510y

---

CITATIONS

7

---

READS

24

3 AUTHORS, INCLUDING:



Kerim Samedov

University of British Columbia - Vancouver

14 PUBLICATIONS 105 CITATIONS

SEE PROFILE

# Facile Molecular Approach to Transparent Thin-Film Field-Effect Transistors with High-Performance Using New Homo- and Heteroleptic Indium(III)–Tin(II) Single-Source Precursors

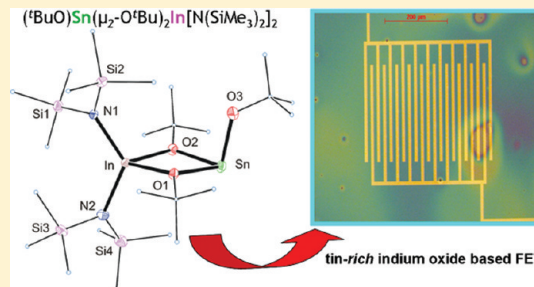
Kerim Samedov, Yilmaz Aksu, and Matthias Driess\*

Institute of Chemistry: Metalorganics and Inorganic Materials, Technische Universität Berlin, Sekr. C2, Strasse des 17 Juni 135, D-10623 Berlin, Germany

## Supporting Information

**ABSTRACT:** Various routes to new molecular bimetallic indium(III)–tin(II) alkoxides precursors for low-temperature synthesis of conducting tin-rich indium tin oxide were investigated. The studies include the facile syntheses, spectroscopic properties, and structural characterization of the new homo- and heteroleptic bimetallic alkoxides  $(^t\text{BuO})\text{Sn}(\mu\text{-O}^t\text{Bu})_2\text{InX}_2$  ( $\text{X} = \text{O}^t\text{Bu}$  (**1**),  $\text{N}(\text{SiMe}_3)_2$  (**2**)) as well as the first heptanuclear bimetallic chlorides, that is, the oxo *tert*-butoxide clusters  $\text{In}_3\text{Sn}_4(\text{O}^t\text{Bu})_6\text{Cl}_6\text{O}_2^{+}\text{Cl}^{-}$  (**3**) and  $\text{In}_3\text{Sn}_4(\text{O}^t\text{Bu})_6\text{Cl}_7\text{O}_2^{+}\text{In}_3\text{Sn}_4(\text{O}^t\text{Bu})_7\text{Cl}_6\text{O}_2$  (**4**). To evaluate the suitability of **1** and **2** as single-source precursors (SSPs) for the preparation of tin-rich indium tin oxide (ITO) thin films, their thermal degradation under dry synthetic air was investigated and the resulting materials were analyzed by a combination of different analytical techniques such as powder X-ray diffraction analysis (PXRD), transmission electron microscopy (TEM), FT-IR, scanning electron microscopy (SEM), energy-dispersive X-ray analysis EDX, elemental analysis, and inductively coupled plasma optical emission spectrometry (ICP-OES). Thermal treatment of **1** and **2** resulted in amorphous tin-rich ITO and crystalline ITO with traces of the cassiterite phase of tin dioxide. Incorporation of tin into the indium oxide lattice on atomic scale in crystalline ITO is evidenced by the increased lattice parameters extracted from the PXRD measurements. Results of the SEM-mapping show homogeneous distribution of indium and tin in the materials. The final In:Sn ratio of the as-prepared materials as determined by means of the ICP-OES analysis is close to that of the In:Sn ratio of 1:1 in the molecular precursors, thus confirming the suitability of **1** and **2** as SSPs to produce tin-rich ITO. Thin film field effect transistors were fabricated by spin-coating of Si-wafers with a solution of **2** in toluene and subsequent calcination under dry air. The as-prepared FETs from **2** exhibit excellent performance as shown by a field effect mobility of  $3.7 \times 10^{-1} \text{cm}^2 \text{V}^{-1} \text{s}$  at  $350^\circ \text{C}$  and an  $I_{\text{on/off}}$  current ratio of  $1 \times 10^7$ .

**KEYWORDS:** molecular precursors, metal oxides, semiconductors, alkoxides, nanocomposites



## INTRODUCTION

Semiconductor oxide materials such as zinc oxide, tin oxides, indium oxide, and tin-doped indium oxide (ITO) are essential materials for the optoelectronic industry, because they combine optical transparency in the visible region with a controllable electrical conductivity. The most widely used TCO in optoelectronics is tin-doped indium oxide (ITO, 5–15 mol % Sn).<sup>1</sup> ITO combines the best to date available performance in terms of conductivity, transparency in the visible and reflectivity in the infrared region with high scratch resistance, thermal stability, chemical inertness, and good surface morphology.<sup>2</sup> Because of these properties, today ITO is the state-of-the-art material in the flat panel display technology<sup>3</sup> as well as the basic material of choice for a vast variety of other applications,<sup>1a,2</sup> including functional glasses,<sup>4</sup> photovoltaics,<sup>5</sup> gas sensing,<sup>6</sup> organic LEDs,<sup>7</sup> and energy-efficient windows.<sup>8</sup> ITO is usually employed in form of thin films deposited using various methods such as magnetron sputtering,<sup>9</sup> reactive evaporation,<sup>10</sup> spray pyrolysis,<sup>11</sup> pulsed laser deposition,<sup>12</sup> and chemical vapor

deposition (CVD).<sup>13</sup> All these processing approaches have apparent disadvantages with respect to the influence of the substrate structures, required high calcination temperatures, extent of control over materials' properties and complexity of the equipment and expenses required. Alternatively, the sol–gel approach<sup>14</sup> combined with spin- and dip-coating as well as several other wet-chemical deposition techniques<sup>15</sup> described in literature were successfully employed in the preparation of ITO coatings.

It is, however, noteworthy that the low abundance of indium and the resulting high price of the materials severely limit the possibilities of using ITO for large-scale industrial production thus prompting intensive efforts to develop new low-cost alternative materials in order to meet the growing demand. Given that generally, for both thin films and nanoscaled ITO

Received: February 15, 2012

Revised: April 19, 2012

Published: May 16, 2012

powder, the preparation method and the tin concentration in the material strongly influence the optical and electrical properties, the development of new facile and efficient approaches to indium tin oxide materials with reduced indium content is highly desirable and of great commercial interest. Also, because the solubility of tin in the  $\text{In}_2\text{O}_3$  lattice is known to depend on temperature,<sup>16</sup> a low-temperature procedure for the preparation of ITO thin films with higher doping rates is necessary. Recently, we showed<sup>17</sup> that following the single-source precursor (SSP) concept, the incorporation of tin into ITO can be accomplished to a much higher degree than in various ITO materials known in the literature. Thermal degradation of the molecular precursor indium(I) tin(II) tritert-butoxide (ITBO) at 400 °C yields tin-rich ITO films displaying high conductivity and durable electro-optical performance. A literature survey revealed that to date there is only one further report<sup>18</sup> on preparation of the tin-rich ITO nanomaterial with comparably high tin-incorporation ratio using a more drastic gas-phase synthetic approach.

The single-source precursor (SSP) concept possesses a valuable bottom-up-approach for the preparation of mixed-metal oxide materials.<sup>19</sup> This approach employs thermal degradation at relatively low temperatures of metastable organometallic compounds containing all elements necessary for the formation of the final solid material in a well-defined ratio, thus allowing a strict control over chemical composition and ensuring their high dispersion in the resulting material.

In our group, a number of metal–organic single-source precursor (SSP) compounds has been synthesized, characterized, and successfully utilized for preparation of a wide range of different heterobimetallic oxide materials.<sup>17,20</sup>

Even though easily accessible, the ITBO precursor is extremely air- and moisture-sensitive and relatively labile, even under inert conditions; this prompted us to develop more reliable indium tin alkoxide-based alternatives suitable as SSPs for preparation of thin tin-rich ITO films. Because the intrinsic lability of ITBO is mainly due to the presence of indium in its less stable low oxidation state (1+), we assumed that indium tin alkoxides bearing indium in the common oxidation state (3+) will increase the stability of the system and decrease its air- and moisture-sensitivity thus being ideally suitable as SSPs for preparation of tin-rich ITO films. A literature survey revealed that there is only one report<sup>21</sup> on synthesis and structural characterization of a heteroleptic indium(III)–tin(II) alkoxides by Veith et al. This encouraged us to explore new synthetic routes to synthesize new homo- and heteroleptic indium(III) tin(II) alkoxides.

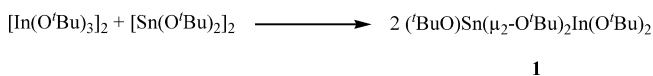
Here we report on the synthesis, spectroscopic characterization and X-ray crystal-structure analysis of the new homo- and heteroleptic bimetallic indium(III)–tin(II) alkoxo compounds **1** and **2** as well as the first isomeric heptanuclear bimetallic indium tin oxo-alkoxide chloride clusters **3** and **4**. We also assess the potential of **1** and **2** as suitable SSPs for deposition and low-temperature preparation of tin-rich ITO thin films.

## RESULTS AND DISCUSSION

**Synthesis and Properties of Compounds 1–4.** The ability of different metal alkoxides to form even mixed heterometallic clusters is well-known.<sup>22</sup> A vast number of molecular homo- and heterometallic alkoxides of various metals have been synthesized following the Lewis acid–base principle.<sup>23</sup> Given our interest in the synthesis of bimetallic

indium(III)–tin(II) alkoxides, we probed whether the Lewis acid–base reaction outlined in Scheme 1 would lead to formation of the mixed heterobimetallic alkoxide **1**.

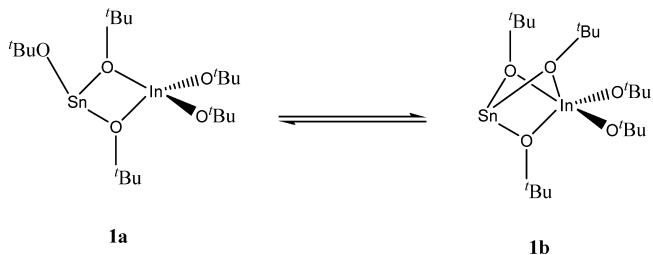
### Scheme 1. Synthesis of **1**



In fact, reacting  $\text{Sn}(\text{O}^t\text{Bu})_2$  and  $\text{In}(\text{O}^t\text{Bu})_3$  in an equimolar ratio in THF and refluxing the reaction mixture for one hour leads to formation of **1** as evidenced by the appearance of a new resonance at  $\delta = -201$  ppm in the  $^{119}\text{Sn}$ -NMR spectrum (see the Supporting Information, SI-1c). Removal of all volatile components in vacuo yields **1** as a colorless solid in quantitative yield. Compound **1** is a thermally stable, low-melting and moderately air- and moisture-sensitive material that is very good soluble in hydrocarbons and nonprotic coordinating solvents. While **1** is indefinitely stable in solutions at room temperature under an inert atmosphere, it turns very slowly into yellowish oil upon prolonged storage as a solid. It has been fully characterized by multinuclear NMR (see the Supporting Information, SI-1a–c), IR, MS (see the Supporting Information SI-1d) and elemental analysis.

The EI mass spectrum of **1** exhibits a intense peak with the characteristic tin isotope pattern at  $m/z = 527$ , assignable to the molecular ion. The room temperature  $^1\text{H}$  NMR and  $^{13}\text{C}$  NMR spectra of **1** in  $\text{C}_6\text{D}_6$  solutions exhibit time-averaged resonances, indicating highly fluxional behavior. The  $^1\text{H}$  NMR spectrum displays 2 sharp resonances at  $\delta = 1.39$  and 1.45 ppm and a broad signal at 1.57 ppm in the integrated ratio of 4:1:5. Although the broad resonance can be assigned to the bridging  $^t\text{BuO}$  ligands, the sharp sets of resonances are attributed to the terminal  $^t\text{BuO}$  groups. The integration ratio can be rationalized by assuming the equilibrium between **1a** and **1b** as depicted in Scheme 2. This has been proven by

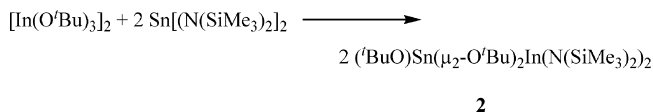
### Scheme 2. Assumed Equilibrium between **1a** and **1b**



variable temperature  $^1\text{H}$  NMR spectroscopy. The  $^{119}\text{Sn}$  NMR spectrum shows even at low temperature only one singlet, indicating that the difference of the chemical shifts of **1a** and **1b** are very small. The chemical shift at  $\delta = -201$  ppm is indicative of three-coordinate tin(II) species.

In an analogous reactions we learned that sterically more hindered tin(II) compounds can also be employed to form tin(II)–indium(III) heteroaggregates. Thus, as outlined in Scheme 3, the reaction of  $\text{In}(\text{O}^t\text{Bu})_3$  with  $\text{Sn}[\text{N}(\text{SiMe}_3)_2]_2$  in an equimolar ratio in THF lead to the desired compound **2** which could be isolated as colorless solid in almost quantitative yield. The constitution of **2** has been deduced from  $^1\text{H}$ -,  $^{13}\text{C}$ -,  $^{29}\text{Si}$ - and  $^{119}\text{Sn}$ -NMR spectroscopy (see Experimental Section and the Supporting Information, SI-2a–d). Recrystallization of **2**

## Scheme 3. Synthesis of 2



in hexane at  $-20^\circ\text{C}$  afforded single crystals suitable for a X-ray structural analysis. Accordingly, **2** is a heterometallic heteroleptic alkoxide amide with two bridging  $^t\text{BuO}$  groups and terminal  $\text{N}(\text{SiMe}_3)_2$  ligands at the  $\text{In}(\text{III})$  atom (Figure 1). The

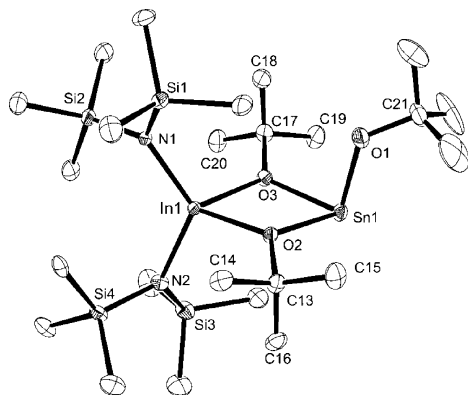


**Figure 1.** Molecular structure of **2**. Thermal ellipsoids are drawn at the 50% probability level. Hydrogen atoms are omitted for clarity. Symmetry transformations used to generate equivalent atoms: I  $x, y, z$ ; II  $-x + 1/2, -y, z + 1/2$ ; III  $x + 1/2, -y + 1/2, -z$ ; IV  $-x, y + 1/2, -z + 1/2$ ; V  $-x, -y, -z$ ; VI  $x - 1/2, y, -z - 1/2$ ; VII  $-x - 1/2, y - 1/2, z$ ; VIII  $x, -y - 1/2, z - 1/2$ .

formation of **2** implies a ligand exchange between  $\text{In}(\text{O}^t\text{Bu})_3$  and  $\text{Sn}[\text{N}(\text{SiMe}_3)_2]_2$ . Obviously **2** is the preferred product because the sterically more demanding  $\text{N}(\text{SiMe}_3)_2$  groups occupy terminal positions.

Similarly as **1**, compound **2** is a colorless, low-melting and moderately air- and moisture-sensitive substance with a very good solubility in all common nonprotic organic solvents. In contrast to the spectroscopic features of **1** in solutions, which indicate highly fluxional behavior, the respective VT  $^1\text{H}$  and  $^{13}\text{C}$  NMR spectra show that **2** is rigid in solutions. The  $^1\text{H}$  spectrum consists of four distinct resonances in the integrated ratio of 2:2:1:2. While the upfield shifted signals at  $\delta = 0.40$  and  $0.45$  ppm with the integrated ratio of 2:2 lie in the range typically observed for  $\text{N}(\text{SiMe}_3)_2$  ligands, thus indicating the presence of two different  $\text{N}(\text{SiMe}_3)_2$  groups in the molecule, the two further downfield-shifted resonances at  $\delta = 1.34$  and  $1.44$  ppm with the integrated ratio 1:2 are located in the range characteristic of  $^t\text{BuO}$  groups in different coordinating environments. Based on the integration ratio of 2:1 in the  $^1\text{H}$  spectrum of **2** and crystal structure data we assign the rather broad resonance at  $\delta = 1.44$  ppm to the bridging  $^t\text{BuO}$  groups, whereas the sharp resonance at  $\delta = 1.34$  ppm is attributed to the terminal  $^t\text{BuO}$  group at the tin(II) atom. The  $^{13}\text{C}$  NMR spectrum of **2** (see Supporting Information, SI-2b) shows three sets of signals corresponding to the  $\text{N}(\text{SiMe}_3)_2$  methyl groups with the expected upfield shift of  $\delta = 7.23$  ppm and terminal as well as bridging  $^t\text{BuO}$  groups further downfield. Typically, as in **1**, the resonances of the primary and quaternary carbon atoms of the bridging  $^t\text{BuO}$  groups are relatively broad. The presence of two different  $\text{N}(\text{SiMe}_3)_2$  groups in the molecule is further corroborated by the appearance of two resonances in the  $^{29}\text{Si}$

NMR spectrum (see Supporting Information, SI-2c) at  $\delta = 2.17$  and  $2.37$  ppm, respectively. The  $^{119}\text{Sn}$ -NMR spectrum (see Supporting Information, SI-2d) exhibits a singlet at  $\delta = -189$  ppm, which is comparable to the chemical shift of  $\delta = -201$  ppm observed for **1** and falls into the range common for three-coordinated tin(II) species.

The EI mass spectrum of **2** (see Supporting Information SI-2e) displays an intensive fragment peak at  $m/z = 759$ , corresponding to the molecular-ion peak with the loss of one methyl group. The assigned composition of **2** was further corroborated by a satisfactory elemental analysis.

Given that there is only a minor difference in the Lewis acidity of the metal centers [ $\text{Sn}(\text{II})$  and  $\text{In}(\text{III})$ ] we were intrigued by the unexpected high stability of the Lewis donor–acceptor adducts **1** and **2**. Thus, we set out to explore the reactivity of indium(III) *tert*-butoxide toward other tin(II) compounds.  $\text{Sn}(\text{O}^t\text{Bu})_3\text{InCl}_2 \cdot \text{THF}$  (**3a**) and its bromine homologue  $\text{Sn}(\text{O}^t\text{Bu})_3\text{InBr}_2 \cdot \text{THF}$  (**3b**) are to date the only two examples of heteroleptic indium(III)–tin(II) alkoxides reported in literature.<sup>21</sup> They were accessible by salt metathesis reaction of  $\text{Na}_2\text{Sn}_2(\text{O}^t\text{Bu})_6$  with  $\text{InCl}_3$  and  $\text{InBr}_3$ , respectively, in refluxing THF. Following our protocol we probed whether the reaction of indium(III) *tert*-butoxide with tin(II) chloride in THF in the molar ratio of 1:1 leads via ligand exchange to **3a**. The reaction was carried out at room temperature and gave a microcrystalline crude product. The latter is soluble in THF, scarcely soluble in aromatic but insoluble in nonaromatic hydrocarbons. Its  $^{119}\text{Sn}$  NMR spectrum in THF- $d_8$  (see the Supporting Information SI-3c) displays one sharp resonance at  $\delta = -300$  ppm typical for the presence of three-coordinate tin(II) centers. The  $^1\text{H}$  NMR spectrum (see the Supporting Information SI-3a) exhibits a broad resonance at  $\delta = 0.49$  ppm in addition to the residual solvent peaks. Similarly, the  $^{13}\text{C}$  NMR spectrum consists of a set of signals ( $\delta = 34.78$  and  $76.56$  ppm) in the range typical for *tert*-butoxide groups (see the Supporting Information SI-3b). The solubility of the product and its NMR spectra are clearly different to those of **3a** reported by Veith et al.<sup>21</sup> In fact, a single-crystal X-ray analysis of crystals grown in saturated THF-toluene solutions revealed that the main product is a ion pair consisting of the novel heptanuclear indium(III)–tin(II) chloro-oxo-*tert*-butoxide cluster cation  $[\text{In}_3\text{Sn}_4(\text{O}^t\text{Bu})_6\text{Cl}_6\text{O}_2]^+$  and a chloride counterion. Because of the idealized  $C_{2v}$  symmetry of the molecular cluster cation in **3** two different kinds of *tert*-butoxide groups and thus two sets of resonances in the  $^1\text{H}$  and  $^{13}\text{C}$  NMR spectra are expected. However, the observed spectra are far simpler, most likely because of the minor differences in the chemical environment of the *tert*-butoxide groups in the cationic cluster in **3**. Any kind of fluxional behavior of **3** in solution could be ruled out based on the results of the solid-state  $^{13}\text{C}$  and  $^{119}\text{Sn}$  MAS NMR spectra of **3** (see the Supporting Information SI-3d and SI-3e). As expected, the yield of **3** can be improved by adjusting the stoichiometry of indium and tin components and using tin(II) *tert*-butoxide instead of the indium(III) *tert*-butoxide whose preparation is rather time-consuming and intricate. Monitoring the reaction progress by NMR spectroscopy clearly shows that **3** is formed as sole product through reaction of indium(III) chloride with tin(II) *tert*-butoxide in the molar ratio of 3:5 under otherwise identical conditions (Scheme 4, Figure 2). Compound **3** is a air- and moisture-stable solid that could be obtained as single crystals upon recrystallization in saturated THF solutions in moderate 40% yield.



## Scheme 4. Synthesis of 3

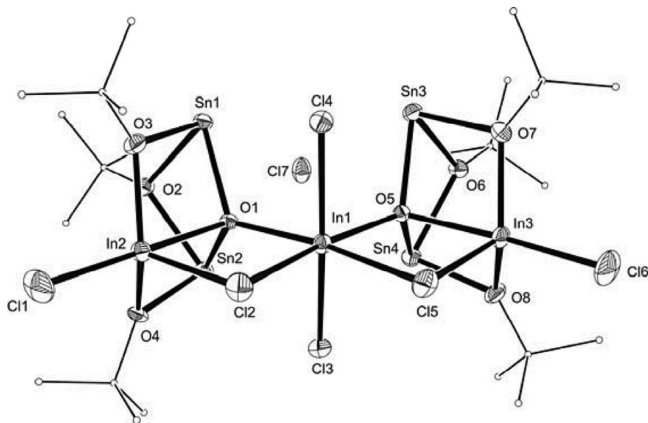
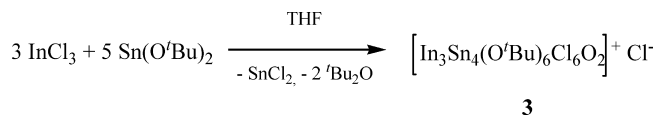
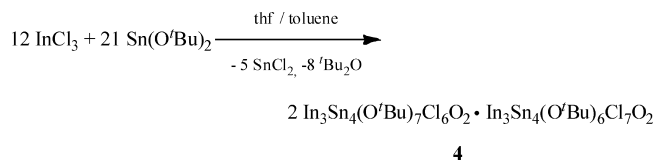


**Figure 2.** Molecular structure of the ion pair **3**. Thermal ellipsoids are drawn at the 50% probability level. Hydrogen atoms are omitted for clarity. The organic substituents have been shown for reasons of clarity only as thin lines. Symmetry transformations used to generate equivalent atoms: I  $x, y, z$ ; II  $-x + 1/2, y + 1/2, -z + 1/2$ ; III  $-x, -y, -z$ ; IV  $x - 1/2, -y - 1/2, z - 1/2$ .

Interestingly, recrystallization of the crude product in tetrahydrofuran-toluene solutions led to small quantities of a side product as indicated by the appearance of an additional broad resonance at  $\delta = -449$  ppm in the  $^{119}\text{Sn}$  NMR spectrum. In order to characterize the aforementioned side product and to examine the influence of toluene on stability and formation of **3**, the latter was redissolved in toluene. A white precipitate was filtered off, the filtrate concentrated and kept at  $-20^\circ\text{C}$  to give colorless plates of the new product **4** in 70% yield. Crystals of **4** dissolved in  $\text{C}_6\text{D}_6$  reveal a broad resonance at  $\delta = -449$  ppm in the  $^{119}\text{Sn}$  NMR spectrum (see the Supporting Information SI-4c) similar to the aforementioned resonance of the side product. The result of the X-ray structural analysis revealed that **4** is an equimolar mixture of the two neutral heptanuclear indium(III)–tin(II) oxo *tert*-butoxide clusters  $\text{In}_3\text{Sn}_4(\text{O}^t\text{Bu})_6\text{Cl}_7\text{O}_2$  (**4a**) and  $\text{In}_3\text{Sn}_4(\text{O}^t\text{Bu})_7\text{Cl}_6\text{O}_2$  (**4b**) (Scheme 5, Figure 3). Compound **4a** is a constitutional isomer of **3**. Attempts to separate **4a** and **4b** by fractional crystallization were unsuccessful.

## Scheme 5. Synthesis of 4



The composition of **4** was further corroborated by a satisfactory elemental analysis. The ambient-temperature  $^1\text{H}$  and  $^{13}\text{C}$  NMR spectra (see the Supporting Information SI-4a and SI-4b) are indicative of a stereochemically rigid behavior displaying the presence of several *tert*-butoxide groups in different coordinating environments. The room-temperature  $^1\text{H}$  NMR spectrum exhibits four singlets, integrating in a ratio

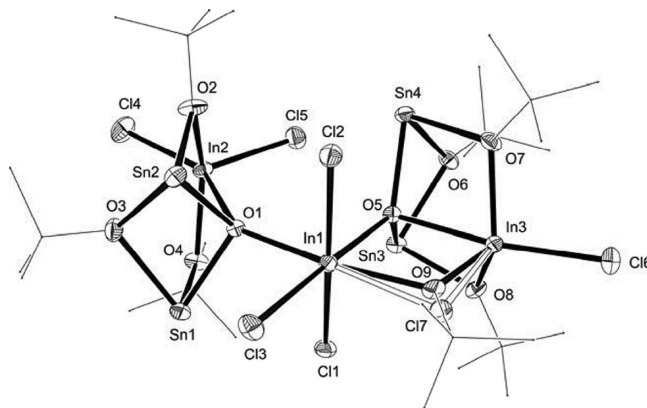


**Figure 3.** Molecular structure of **4** (1:1 mixture of **4a** and **4b**): Hydrogen atoms are omitted for clarity. An equatorial position at In3 was refined as equally occupied by a *tert*-butoxy group ( $\text{O}^t\text{Bu}$ ) and a chloro ligand (Cl7). The organic substituents have been shown for reasons of clarity only as thin lines. Thermal ellipsoids are drawn at the 50% probability level. Symmetry transformations used to generate equivalent atoms: I  $x, y, z$ ; II  $-x, y, -z + 1/2$ ; III  $x + 1/2, y + 1/2, z$ ; IV  $-x + 1/2, y + 1/2, -z + 1/2$ ; V  $-x, -y, -z$ ; VI  $x, -y, z - 1/2$ ; VII  $-x + 1/2, -y + 1/2, -z$ ; VIII  $x + 1/2, -y + 1/2, z - 1/2$ .

of 2:2:3:6. Given the  $C_s$  symmetry of both components of **4** at least nine resonances would be expected. The significantly reduced number of observable signals is most likely due to the coincidence of some resonances because of very similar bonding features of **4a** and **4b**. Likewise, the  $^{13}\text{C}$  NMR spectrum of **4** displays four sets of resonances for the *tert*-butoxy groups.

The structural integrity of the oxo-alkoxy-bridged heterobimetallic cores of **3** and **4**, respectively, in solutions is proven by comparison of the respective solid state  $^{13}\text{C}$  and  $^{119}\text{Sn}$  MAS NMR spectra with the spectra obtained in solutions (see the Supporting Information SI-3c, SI-3e, SI-4c and SI-4e). Both compounds display similar chemical shifts in solutions ( $\delta = -300$  ppm for **3**,  $\delta = -449$  ppm for **4**) and in the solid state ( $\delta = -282$  ppm for **3**,  $\delta = -475$  ppm for **4**).

**Structural Elucidation of 2–4.** The solid state structure of **2** is shown in Figure 1. Selected bond lengths and angles are given in the Supporting Information, SI-Table-1 and SI-Table-2. Compound **2** crystallizes orthorhombic in the space group  $Pbca$  with eight molecules in the unit cell. The molecules of **2** possess a mirror plane passing through Sn1, In1, O1, N1, and N2 atoms (point group symmetry:  $C_s$ ). The solid state structure of **2** shows an almost planar  $\text{InO}_2\text{Sn}$  ring with two bridging *tert*-butoxide groups, two terminal hexamethylsilazane ligands bonded to the distorted tetrahedral coordinate In atom, and a terminal *tert*-butoxide group bonded to the  $\psi$ -trigonal pyramidal coordinate Sn atom. The endocyclic In–O distances ( $\text{In1–O2} = 213.8(3)$ ,  $\text{In1–O3} = 214.2(3)$  pm) in **2** are little longer than the In–O bond lengths observed for other indium alkoxides. The Sn–O ( $\text{Sn1–O2} = 215.6(3)$ ,  $\text{Sn1–O3} = 215.4(3)$  pm) bond lengths in the  $\text{InO}_2\text{Sn}$  ring in **2** are virtually equal. The endocyclic O2–In1–O3 angle in **2** is slightly smaller ( $73.8^\circ$ ) than those observed in homo- and heteroleptic homometallic In(III) alkoxides with a  $\text{M}_2\text{O}_2$  ring,<sup>24</sup> whereas the O–Sn–O angle ( $\text{O2–Sn1–O3} = 73.2(1)^\circ$ ) is almost identical to those reported for homo- and heteroleptic homometallic Sn(II) alkoxides bearing a  $\text{M}_2\text{O}_2$  ring.<sup>24c,d</sup> Accordingly, the  $\text{In1–O1–Sn1}$  and  $\text{In1–O2–Sn1}$  bond angles are essentially similar ( $106.13(12)^\circ$  and  $106.05(12)^\circ$ ). The

bridging oxygen atoms in **2** are almost trigonal-planar coordinated ( $354.4^\circ$ ) and thus close to  $sp^2$ -hybridization. The Sn–O distances to the bridging oxygen atoms in **2** are essentially identical ( $\sim 200.0(3)$  pm). The angle between the plane comprising the  $\text{InO}_2\text{Sn}$  ring (Sn1–In1 vector) and the terminal *tert*-butoxide ligand at the tin atom in **2** is relatively large ( $98.7^\circ$ ) and differs from the acute angle ( $\sim 86.4^\circ$ ) observed in homo- and heteroleptic homometallic In(III) and Sn(II) alkoxides with a  $\text{M}_2\text{O}_2$  ring, respectively.<sup>24c,d</sup> This widening can be attributed to the increased repulsive interactions between the terminal ligands at the respective metal centers. The In–N bond lengths (In1–N1 =  $208.1(3)$  pm, In1–N2 =  $208.4(4)$  pm) are essentially equal and similar to the values observed for related indium amides.<sup>24,25</sup> The staggered conformation of the bridging *tert*-butoxide groups and the orientation of the terminal *tert*-butoxide group away from the  $\text{InO}_2\text{Sn}$  plane reduces repulsive interactions in the molecule.

The molecular structure of **3** is shown in Figure 2; selected bond lengths and angles are given in the Supporting Information, SI-Table-3 and SI-Table-5.

The compound crystallizes monoclinic in the space group  $P2_1/n$  with four molecules per unit cell. It consists of an ion pair bearing a novel heptanuclear indium(III)-tin(II) oxo *tert*-butoxide cluster cation with approximately  $C_{2v}$  symmetry and a chloride counterion. The two  $\text{InSn}_2\text{O}_4$  subunits of the metal-oxo core represent distorted cubane-like frameworks with a missing corner, bound symmetrically to the central octahedral coordinate indium atom (In1). The central In1 atom bears two chloro atoms (Cl3, Cl4) in axial positions and two chloro ligands (Cl2, Cl5), bridging In1 with In2 and In3, respectively, as well as the two aforementioned oxo ligands ( $\mu_4$ -O1,  $\mu_4$ -O5) comprising the planar equatorial plane. The  $\text{InSn}_2\text{O}_4$  subunits consist each of an indium atom in a slightly distorted trigonal-bipyramidal environment linked by an oxo ligand in the axial position and a bridging *tert*-butoxide group to one tin atom as well a second *tert*-butoxide group to another tin atom in equatorial positions. A bridging chloro atom as well as a further terminal chloro atom in the axial position complete the trigonal-bipyramidal environment of the respective indium atom in each  $\text{InSn}_2\text{O}_4$  core. The tin atoms (Sn1, Sn2 and Sn3, Sn4) are both distorted trigonal-pyramidal coordinated consisting of oxo ligands and two bridging *tert*-butoxide groups. The oxo ligands O4 and O5 are each distorted tetrahedral coordinated by two tin atoms and two indium atoms, one of which belongs to the corresponding  $\text{InSn}_2\text{O}_4$  subunit with the other one being the central indium atom In1.

The octahedral arrangement around In1 is only slightly distorted from the ideal octahedral geometry as can be deduced from the bond angles. The indium atom In1 lies in the equatorial plane of the octahedron ( $\sum$  of angles of In1  $360.0^\circ$ ) and the Cl3–In1–Cl4 angle deviates by less than  $12^\circ$  from  $180^\circ$ . The corresponding Cl4–In1–Cl2 ( $92.9(9)^\circ$ ) and Cl4–In1–Cl5 ( $95.2(8)^\circ$ ) angles are a little obtuse deviating only slightly from  $90^\circ$ . The Cl4–In1–O5 ( $85.5(4)^\circ$ ) and Cl4–In1–O1 ( $85.9(2)^\circ$ ) angles are in turn somewhat acute and almost equal. They also deviate insignificantly from the ideally expected  $90^\circ$ . The same holds true for the O1–In1–Cl2 ( $81.33(8)^\circ$ ) and O5–In1–Cl5 ( $81.68(8)^\circ$ ) angles. Interestingly, in spite of larger covalent radius of the chlorine atoms (102 pm vs 66 pm for oxygen) the Cl2–In1–Cl5 angle ( $85.91(4)^\circ$ ) is distinctly smaller than the O1–In1–O5 ( $111.09(1)^\circ$ ) angle. The bond lengths within the octahedron

are somewhat unusual since the distances between In1 and equatorial chloro ligands Cl1 and Cl5 are remarkably longer (In1–Cl2 =  $259.2(1)$  and In1–Cl5 =  $256.05(1)$  pm) than usually observed,<sup>26,24j</sup> whereas bond lengths between the In1 and axially positioned chloro atoms Cl3 and Cl4 are at the upper limit of the range (In1–Cl3 =  $246.8(7)$  and In1–Cl4 =  $248.28(1)$  pm). On the other hand, the In– $\mu_4$ O distances (In1–O1 =  $213.4(3)$  pm and In1–O5 =  $215.01(3)$  pm) are unexpectedly short being in the range typically observed for  $\text{In}\mu_2\text{O}$  distances. The bonding parameters of the trigonal-bipyramidal arrangement of the indium atoms in the  $\text{InSn}_2\text{O}_4$  subunits flanking the In1 atom differ from each other only very little and are rather close to common values observed. The In–O bond lengths are in the expected range and clearly display the established tendency observed for  $\text{In–OR} < \text{In–}\mu_2\text{OR} < \text{In–}\mu_3\text{OR} < \text{In–}\mu_4\text{O}$  (In2–O3 =  $209.3(3)$  and In2–O4 =  $210.1(3)$  pm, whereas In2–O1 =  $225.8(3)$  pm). While the O–Sn–O angles of the two trigonal pyramidally configured tin(II) centers present in the  $\text{InSn}_2\text{O}_4$  subunit are virtually equal and fall nicely into the range usually observed for three-coordinated tin(II) species, the Sn– $\mu_2$ –O distances are significantly larger (Sn1–O3 = Sn1–O3 =  $217.2(3)$  pm and Sn2–O2 =  $217.1(3)$ , Sn2–O4 =  $218.5(3)$  pm) than the Sn–O bond lengths found elsewhere in the literature<sup>27</sup> ( $\sim 2.07$  pm). Somewhat unusual are also the rather short Sn– $\mu_4$ –O distances (Sn1–O1 =  $214.7(3)$ , Sn2–O1 =  $214.0(3)$  pm) observed in the  $\text{InSn}_2\text{O}_4$  subunits.

A moderate distortion of the tetrahedral coordination sphere around the oxo ligands O1 and O5 is reflected in the bond angles (In1–O1–Sn1 =  $120.34(1)^\circ$ , In1–O1–Sn2 =  $120.33(1)^\circ$ , Sn1–O1–OIn2 =  $99.95(2)^\circ$ ) deviating perceptibly from the ideal tetrahedral angle. The solid state structure of **4** was established by X-ray crystal structure and the result is shown in Figure 3; the atomic numbering scheme and selected bond lengths and angles are given in the Supporting Information, SI-Table-4 and SI-Table-5.

Compound **4** crystallizes monoclinic in the space group  $C2/c$ . In contrast to the ionic nature of the solid state molecular structure of **3**, **4** is a 1:1 mixture of the two cluster compounds **4a** and **4b**. Both consist of unprecedented neutral heptanuclear indium(III)–tin(II) oxo *tert*-butoxide clusters. Although in **4**, similarly to **3**, all tin atoms are present in an analogous distorted  $\psi$ -trigonal pyramidal environment (vide supra), in contrast to **3**, the three indium atoms in **4** have each a distinct coordination environment. Whereas In1 is octahedral coordinated, In2 has a square pyramidal ligand surrounding, and In3 adopts distorted trigonal-bipyramidal coordination. Akin to **3**, the octahedral coordinate In1 with two chloro atoms (Cl1 and Cl2) in the axial position and two  $\mu_4$ -O oxo ligands (O1 and O5) cis to each other in the equatorial position remains as central metal atom in **4**. Unlike in **3**, in **4**, a terminal chloro ligand (Cl3) and with a 50% probability a bridging chloro ligand (Cl7) and a bridging *tert*-butoxide group, respectively, comprise the perfectly planar equatorial plane and complete the octahedral environment around In1. In1 is linked by the oxo ligand  $\mu_4$ -O5 to an  $\text{InSn}_2\text{O}_4$  subunit, which is the second structural feature **3** and **4** have in common. As in **3**, the indium atom in the  $\text{InSn}_2\text{O}_4$  subunit possesses an identical (vide supra) but distinctly more distorted trigonal-bipyramidal environment. The intrinsic  $C_{2v}$  symmetry of **3** is broken in **4** by the presence of another isomeric  $\text{InSn}_2\text{O}_4$  subunit. Similarly as in **3**, the central indium atom (In3) is out of the equatorial plane ( $\sum$  of angles of In  $341.7(1)^\circ$ ) and slightly shifted toward the terminal

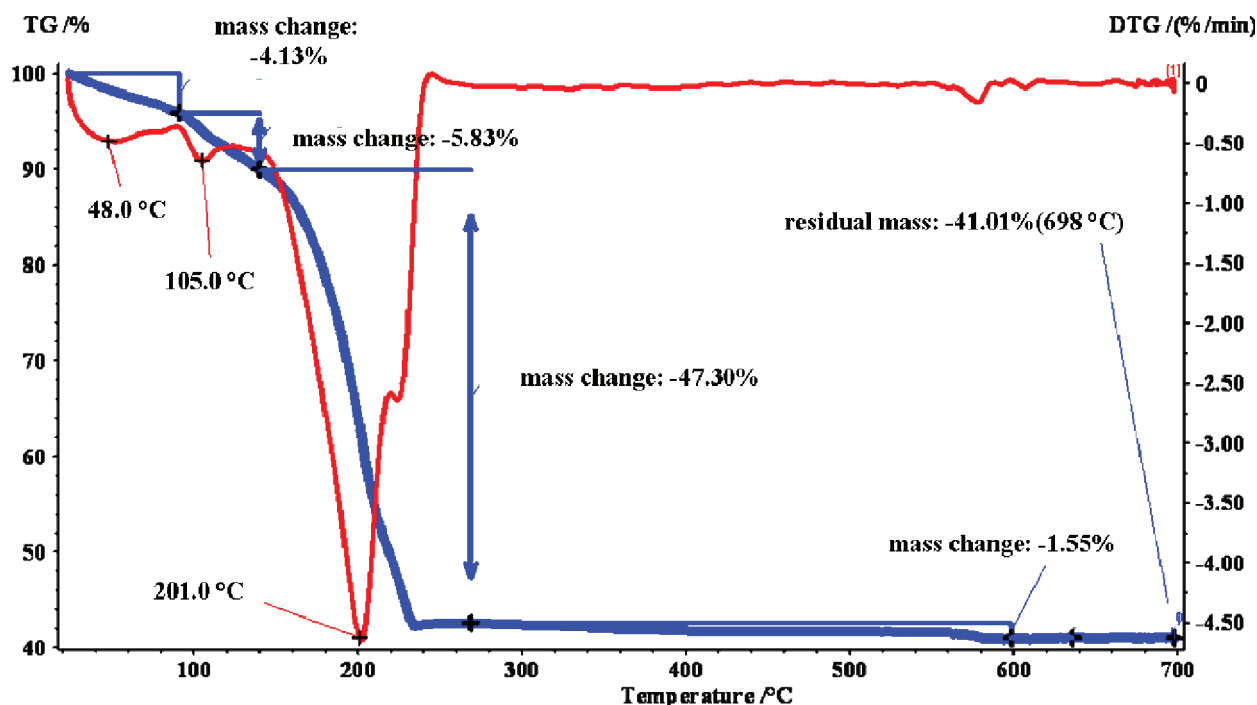


Figure 4. TGA and DTA curves for the degradation of 1 in dry synthetic air with a heating of rate  $5 \text{ K min}^{-1}$ , starting from room temperature to  $700^\circ\text{C}$ .

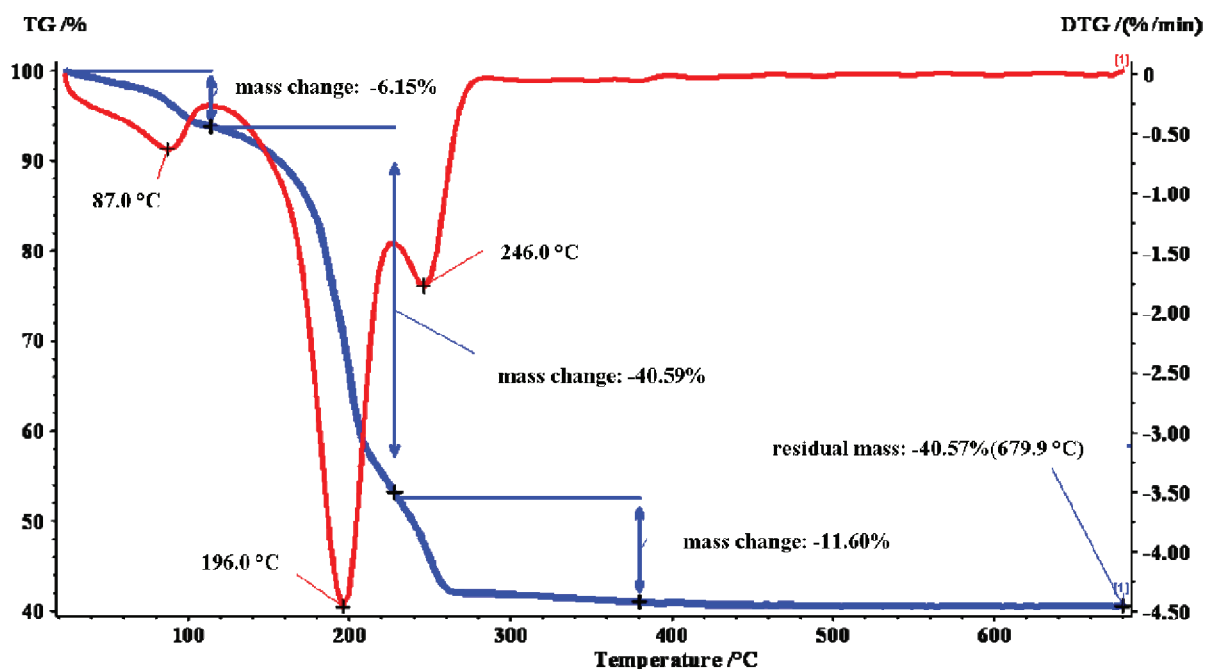
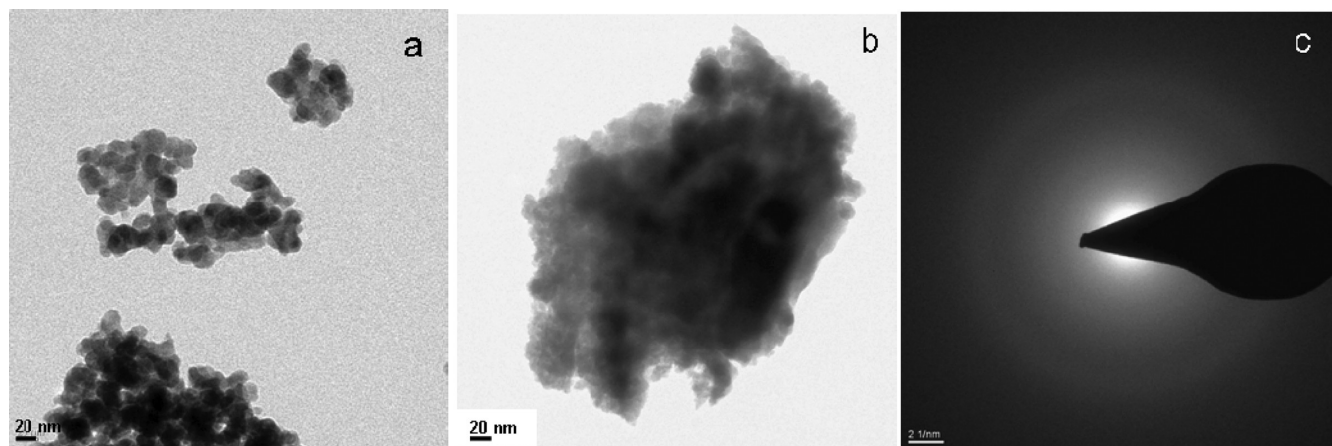


Figure 5. TGA and DTA curves for the degradation of 2 in dry synthetic air with a heating rate of  $5 \text{ K min}^{-1}$ , starting from room temperature to  $700^\circ\text{C}$ .

chloro ligand (Cl6). In contrast to 3, the deviation of the angular parameters from the ideal trigonal bipyramidal geometry in 4 is significantly larger. The O5–In3–Cl6 angle formed by the axially oriented atoms is  $167.72(8)^\circ$  ( $178.5(1)^\circ$  in 3), whereas the ligands in the equatorial positions reveal smaller angles (O8–In3–O9 =  $108.95(1)^\circ$ , O9–In3–O7 =  $104.79(1)^\circ$ , O8–In3–Cl7 =  $107.10(1)^\circ$ , Cl7–In3–O7 =  $112.57(1)^\circ$ ) than the expected value of  $120^\circ$ . Likewise, the respective Cl–In3–O angles (Cl6–In3–O7 =  $100.16(1)^\circ$ ,

Cl6–In3–O8 =  $116.22(1)^\circ$ , Cl6–In3–O9 =  $99.0(1)^\circ$ ) differ strongly from the anticipated angle of  $90^\circ$ .

The In–Cl (In2–Cl4 = 239.6 pm, In2–Cl5 = 240.5 pm) and In–O (In2–O1 = 227.5 pm, In2–O2 = 211.3 pm, In2–O4 = 211.3 pm) bond lengths in the square pyramid around the In2 are comparable with those reported in literature.<sup>24</sup> The somewhat elongated In2–O1 distance might be either caused by the  $\mu_4$  coordination mode of the oxo ligand (O1) or a trans effect exerted by the trans covalently bound chloro atom (Cl4). The distortion of the square pyramidal geometry manifests



**Figure 6.** TEM images of (a) **1** and (b) **2**, and (c) selected-area electron diffraction pattern of the material (tin-rich  $\text{In}_2\text{O}_3$ ) prepared from the degradation of **1** and **2**.

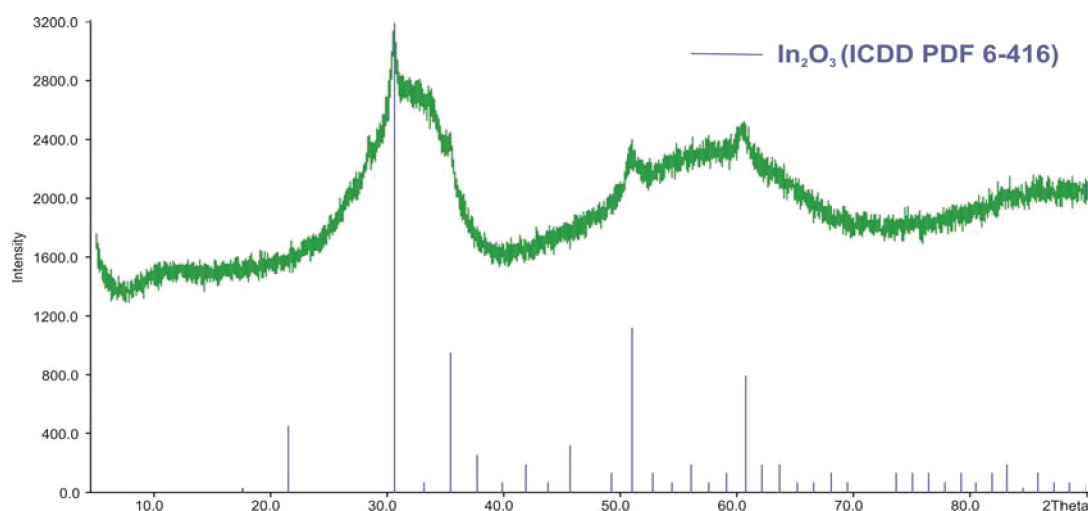


**Figure 7.** PXRD pattern of the material derived from the degradation of **2** in dry synthetic air with a heating rate of  $5 \text{ K min}^{-1}$  from room temperature to  $700^\circ\text{C}$ .

itself most clearly in the deviation of the angular parameters from the ideal values. Because the indium atom In2 is distinctly out of the equatorial plane and shifted toward Cl5, all the Cl5–In2–O<sup>eq</sup> (Cl5–In2–O1 =  $103.45(8)^\circ$ , Cl5–In2–O2 =  $103.43(1)^\circ$ , Cl5–In2–O4 =  $103.28(1)^\circ$ ) angles as well as the Cl5–In2–Cl4 value of  $107.17(5)^\circ$  angle are obtuse. Expectedly, the Cl5–In2–O<sup>eq</sup> angles are almost equal and slightly smaller than the Cl5–In2–Cl4 angle. The same trend can be observed when looking at and comparing the sizes of the O<sup>eq</sup>–In2–O<sup>eq</sup> (O1–In2–O2 =  $74.07(1)^\circ$ , O1–In2–O4 =  $73.81(1)^\circ$ ) and Cl<sup>eq</sup>–In2–O<sup>eq</sup> (Cl4–In2–O2 =  $98.25(9)^\circ$ , Cl4–In2–O4 =  $99.10(9)^\circ$ ) angles.

**Solid-State Degradation of **1** and **2**.** To learn whether the new heterobimetallic compounds **1** and **2** are suitable SSPs for the preparation of tin-doped indium oxide (ITO), at first their thermal properties were investigated. Degradation of **1** was initially investigated by TGA/DTG studies under dry synthetic air (20%  $\text{O}_2$ , 80%  $\text{N}_2$ ) in the temperature range of  $20$ – $700^\circ\text{C}$ . Figure 4 shows the TGA/DTG curves for **1**. They display a gradual loss of weight of 9.96% between 40 and  $105^\circ\text{C}$  followed by a substantial weight loss of ca. 47.3% with an onset temperature of  $110^\circ\text{C}$  and a negligible mass loss of ca.

1.55% between 240 and  $580^\circ\text{C}$ , resulting in a final remaining mass of 41.01%.

Apparently the degradation of **1** is essentially at least a two-step process, during which first the elimination of coordinated THF takes place resulting in a weight loss of 9.96% (10.74% calc.) followed by a rapid and complete oxidative combustion of the organic groups to carbon dioxide and water in the second step, resulting in a weight loss of ca. 47.30% (50.45% calcd). Assuming that the degradation of **1** takes place according to the scheme portrayed in the Supporting Information SI-5, and the remaining material consists solely of the metal oxides ( $\text{SnO}_2$ ,  $\text{In}_2\text{O}_3$ ) as indicated by elemental analysis (C, H content <0.4%) and powder X-ray diffraction pattern (see the Supporting Information SI-6) the calculated remaining mass shall amount to 43.13%, which is in good agreement with the experimentally observed remaining mass of 41.01%.

Contrary to the proposed two-step degradation process of **1**, the thermal degradation of **2** consists apparently of three different processes, as becomes evident from the TGA/DTG curves depicted in Figure 5. The DTG curve shows two local minima at 87 and  $246^\circ\text{C}$  as well as a global one at  $196^\circ\text{C}$  representing the main step of the thermal degradation taking place in the temperature range of  $120$ – $230^\circ\text{C}$ . As may be



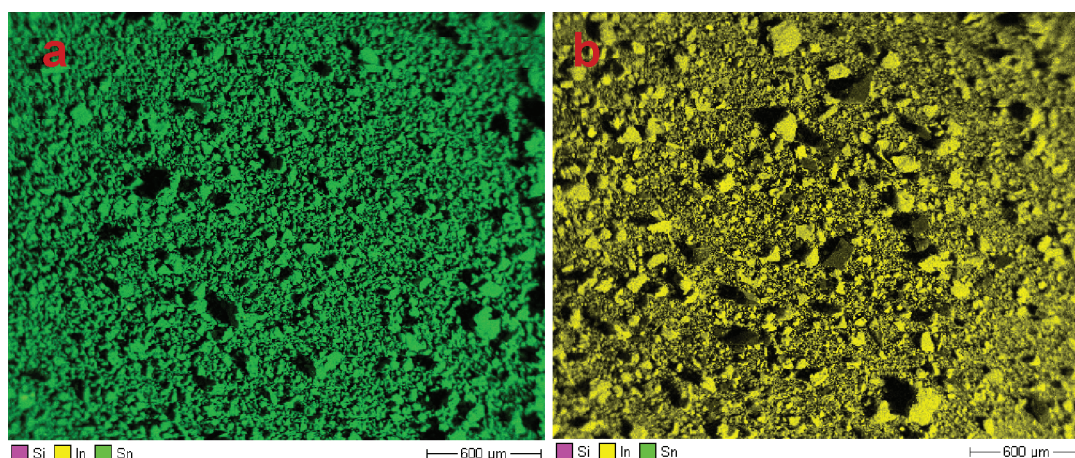


**Figure 8.** EDX mapping SEM images showing the (a) tin and (b) indium dispersion in the as-prepared material from the degradation of **2** in dry synthetic air with a heating rate of  $5\text{ K min}^{-1}$  from room temperature to  $700\text{ }^{\circ}\text{C}$ .

deduced from the experimentally observed remaining mass (40.57%) the second step of the degradation of **2** is rather a thermally triggered elimination of the hexamethyldisilazane ligands, presumably as corresponding “free” amine, than an oxidation (see the Supporting Information SI-7). This is supported by comparison of observed (40.59%) vs calculated (41.46%) values of weight loss.

Although it remains not entirely clear what happens mechanistically in the previous ( $25\text{--}120\text{ }^{\circ}\text{C}$ , weight loss of 6.15%) and in the following steps ( $230\text{--}380\text{ }^{\circ}\text{C}$ , weight loss of 11.60%), they are both associated with respect to complete oxidation of the remaining organic groups as suggested by the satisfactory results of the elemental analysis of the material (C, H content  $<0.4\%$ ) and reasonable agreement between calculated (37.42%) and observed remaining masses (40.57%).

The discrepancy of +3.15% might be attributed to a negligibly small partial oxidation of the hexamethyldisilazane groups yielding silicon dioxide as the only nonvolatile oxidation product, thus adding to the remaining mass. Decomposition of both **1** and **2** under standard conditions ( $20\%\text{ O}_2 + 80\%\text{ N}_2$ ; heating rate of  $5\text{ K min}^{-1}$ ;  $25\text{ to }700\text{ }^{\circ}\text{C}$ , 2 h) afforded slightly yellow colored powder materials which were characterized further by PXRD, TEM, EDX and ICP-OES analysis. Remarkably, despite identical degradation conditions and comparable temperature ranges ( $25\text{--}250\text{ }^{\circ}\text{C}$  for **1** and  $25\text{--}280\text{ }^{\circ}\text{C}$  for **2**) the materials differ significantly in their consistency, as evidenced by their morphology (Figure 6) and powder X-ray diffraction patterns (Figure 7 and Supporting Information SI-6). Although the powder XRD pattern of the material as-prepared by degradation of **1** indicates its highly crystalline nature and matches well with those of the standard cubic bixbyite indium oxide (JCPDS no. 06–0416), the XRD of the degradation product of **2** shows a pattern typical of an amorphous material with a few reflexes indicating the presence of a crystalline indium oxide (JCPDS no. 06–0416) phase. Alongside with the typically shifted and broadened indium oxide reflexes the PXRD pattern of the material derived from the degradation of **1** displays an additional reflex assignable to the cassiterite (JCPDS no. 71–0652) crystalline phase of tin dioxide.

The TEM images shown in Figure 6 support the findings derived from PXRD (see Figure 7 and Supporting Information SI-6). In Figure 6a, the images show agglomerated nonuniform irregularly shaped nanosized particles with diameters varying in

size from 15 to 35 nm for the material obtained by the degradation of **1**. As can be clearly seen from Figure 6b and the SAED pattern in Figure 6c the particles obtained from the degradation of **2** reveal a more amorphous character. The TEM images presented in Figure 6b show the presence of unshaped particles, completely agglomerated with no grain boundaries and vary strongly in size by some 100 nm. The amorphous nature of the material becomes evident from the absence of clear diffraction rings in the SAED pattern (Figure 6c).

The tin content in the as-prepared materials was determined by two different methods: energy-dispersive X-ray analysis and inductive coupled plasma optical emission analysis, and compared with each other. The molar tin–indium ratios in the ITO particles of the materials calculated using the determined tin content values are summarized in the Supporting Information, SI-Table-6.

They are sufficiently coherent and reasonably close to **1** demonstrating the applicability of **1** and **2** as SSPs for preparation of tin-rich ITO materials.

The high dispersion of tin in the decomposition materials is further evidenced by the EDX mapping SEM images shown in Figure 8 and in the Supporting Information, SI-8. Replacement of indium sites in the indium oxide lattice by tin atoms in the material derived from the decomposition of **1** can be deduced from increased lattice parameters extracted from the PXRD measurements. The reflex positions were used to calculate the lattice constant  $a$  ( $10.1591(18)\text{ \AA}$ ) by Werner’s algorithm. Using the same algorithm the lattice constants of the pure indium oxide and industrially manufactured ITO with 5 mol % tin were determined and compared. The comparison shows an unambiguous trend: The lattice constant increases with increasing tin content from  $10.1180(3)\text{ \AA}$  for pure indium oxide over  $10.1214(6)\text{ \AA}$  for the industrially manufactured ITO (Evonik Degussa GmbH) up to  $10.1591(18)\text{ \AA}$  found for our material. This observation is in accordance with the trend reported by Quaas et al.,<sup>28</sup> who attribute the increase in the lattice constant to incorporation of tin ions into the In1 and In2 sites of the indium oxide lattice.

**Thin Film Applications Applying the SSP 2.** Transparent conductive thin films were prepared by spin coating solutions of precursor **1–4** in toluene on precleaned glass substrates under controlled conditions, e.g., in nitrogen atmosphere ( $\text{O}_2 < 1\text{ ppm}$ ,  $\text{H}_2\text{O} < 6\text{ ppm}$ ), followed by thermal treatments in air for 120 min at temperatures ranging from 150

to 450 °C. Subsequently, the obtained coatings were treated for 90 min with a reductive gas mixture (10% H<sub>2</sub>–90%N<sub>2</sub>). Electrical and transmission measurements were made as described in our previous works.<sup>17</sup> The final films obtained from 3 and 4 at a drying temperature of 400 °C showed their best sheet resistances, which were greater than 1000 ohms/square. In contrast, transparent films obtained from 1 and 2 under the same conditions exhibited better electronic properties with sheet resistance ranging from 150 to 300 ohms/square, which are comparable values with those obtained with commercial available ITO coatings. Investigation of the morphologies and electrical properties of the as-prepared films revealed clearly that the films resulting from 2, which showed high homogeneity, good adhesion with the substrate, and the best optoelectronic properties, were more suitable as semiconducting material for TCO applications.

The high solubility of 2 in aprotic organic solvents facilitates the way to processing under fairly mild conditions directly from solutions of the precursor to form semiconductive tin-rich ITO thin films with appreciable film morphology.

As described in the Experimental Section, thin film formation has been performed by spin-coating silicon wafers under controlled inert conditions (O<sub>2</sub> < 1 ppm, H<sub>2</sub>O < 6 ppm) using a solution of 2 in toluene, without any additive or stabilizer, and subsequent thermal treatment of the layers in dry synthetic air at temperatures from 250 to 350 °C. The as-prepared thin layers are very homogeneous and, after thermal treatment, lead to highly compact tin-rich ITO films with flat morphology (see Figures 9 and 10). As confirmed by SEM imaging, the tin-rich

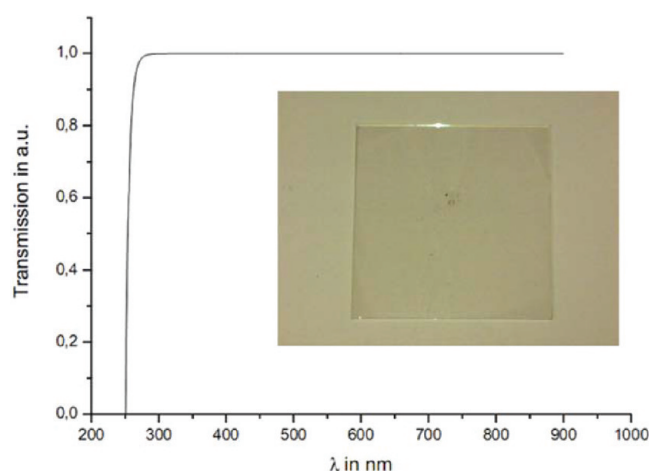


**Figure 9.** Tin-rich ITO-based coating prepared by spin-coating a toluene solution of precursor 2 on glass with subsequent annealing at 350 °C in air and its UV–vis spectrum.

ITO coatings are highly amorphous. Correspondingly, PXRD-studies prove the absence of crystalline material. Based on UV–vis spectra, the as-prepared tin-rich ITO films show transmittance of 98% (Figure 9).

Confocal microscopy images were performed to investigate the morphology of the thin films and they show a compact structure with homogeneous morphology and a very smooth surface (Figures 10a and 10b), especially for the film annealed at 350 °C (Figure 10b).

The resulting thin films (30–50 nm thickness) (Figure 11) obtained after calcination, were transparent and exhibited good adhesion on the Si substrates. The FET (field effect transistor)

substrate consist of heavily doped silicon coated with a 240 nm SiO<sub>2</sub> layer, on which gold electrodes were deposited with an intermediate adhesive of ITO.

The thin film FET were also characterized by SEM mapping, which showed the metals indium and tin to be homogeneously dispersed. Typical SEM images for the sample annealed at 250 and 350 °C are shown in images a and b in Figure 12.

The electronic performance of the as-prepared thin films was studied. Figure 13 (see Table 1 and the Supporting Information SI-9 and SI-10) shows the drain current as a function of drain voltage ( $I_D$ – $V_D$  characteristics) with varied gate voltage ( $V_G$ ) for FET devices.

The TFT performance parameters are summarized in Table 1. The best results were obtained for the sample annealed at 350 °C. The as-fabricated thin film FET operates in the enhanced mode with a threshold voltage of approximately 2 V. It exhibits a saturation electron mobility of  $\mu = 3.7 \cdot 10^{-1} \text{ cm}^2 \text{ V}^{-1} \text{ s}^{-1}$  with an on–off current ratio of  $1 \times 10^7$  (see also the Supporting Information SI-9 and SI-10).

SSP 2-based thin film transistors prepared at 350 °C showed the best FET characteristics. Films as-prepared at temperatures lower than 250 °C were not homogeneous enough probably due to incomplete formation of the metal oxide network, whereas at higher temperatures ( $\geq 350$  °C) cracking was the main problem preventing good film quality and electrical conductivity.

The low temperature degradation of 2 has proven to be a promising method for the preparation of amorphous and tin-rich indium tin oxide thin films with high electron mobility and without grain boundaries. Furthermore, the SSP 2 with its significantly lower processing temperature offers a promising way for the preparation of amorphous and tin-rich indium tin oxide with good FET characteristics, which is a very attractive semiconductor for many electronic devices.

## CONCLUSION

We reported the successful straightforward preparation of the novel homo- and heteroleptic indium(III)–tin(II) complexes 1–4 by a one-pot reaction procedure. Thermal degradation of the complexes 1 and 2 under dry synthetic air give rise to semiconducting halogen-free tin-rich indium tin oxide (ITO) materials, which are highly promising for use in the preparation of thin film field effect transistors. Although the thermal degradation of 1 leads to highly crystalline material, the degradation of 2 affords tin-rich ITO materials with more amorphous character. Thus, thin films prepared from 2 were successfully probed for FET applications. The thin film FET devices produced by spin-coating a solution of 2 in toluene on *n*-doped Si-wafers and subsequent calcination in dry air at 350 °C, revealed high electron mobilities and on/off ratios due to the high homogeneity of the amorphous material and the lack of grain-boundaries.

## EXPERIMENTAL SECTION

**General Considerations.** All experiments and manipulations were carried out under dry oxygen-free nitrogen using standard Schlenk techniques or in an MBraun inert atmosphere glovebox containing an atmosphere of purified nitrogen. Solvents were dried by standard methods and freshly distilled prior to use. InCl<sub>3</sub> was purchased from Sigma-Aldrich, whereas In(O<sup>*i*</sup>Bu)<sub>3</sub>,<sup>21</sup> Sn(O<sup>*i*</sup>Bu)<sub>2</sub>,<sup>29</sup> and Sn[N(SiMe<sub>3</sub>)<sub>2</sub>]<sub>2</sub><sup>30</sup> were prepared according to known literature procedures.

**Preparation of Materials.** Tin-rich ITO materials were prepared by thermal decomposition of 1 and 2 in a quartz tube reactor in



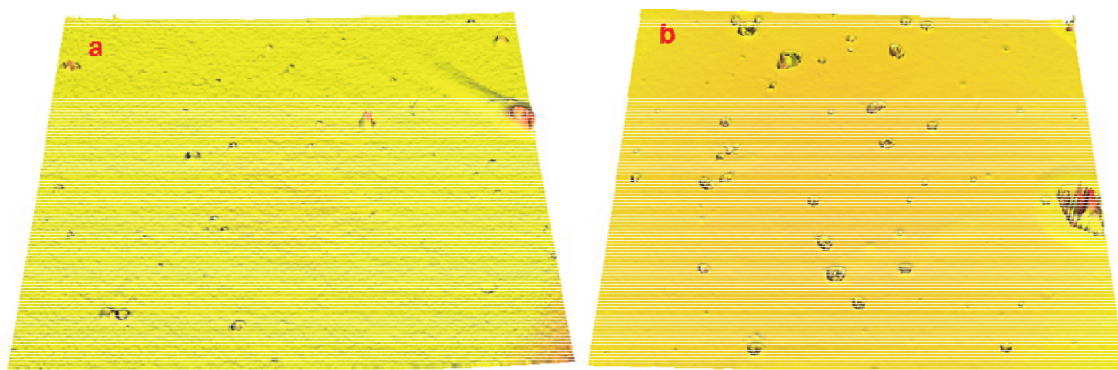


**Figure 10.** Surface topography investigations of the as-prepared tin-rich ITO thin film from **2** grafted on glass after calcination at (a) 250 °C and (b) 350 °C in dry air by means of confocal microscopy.

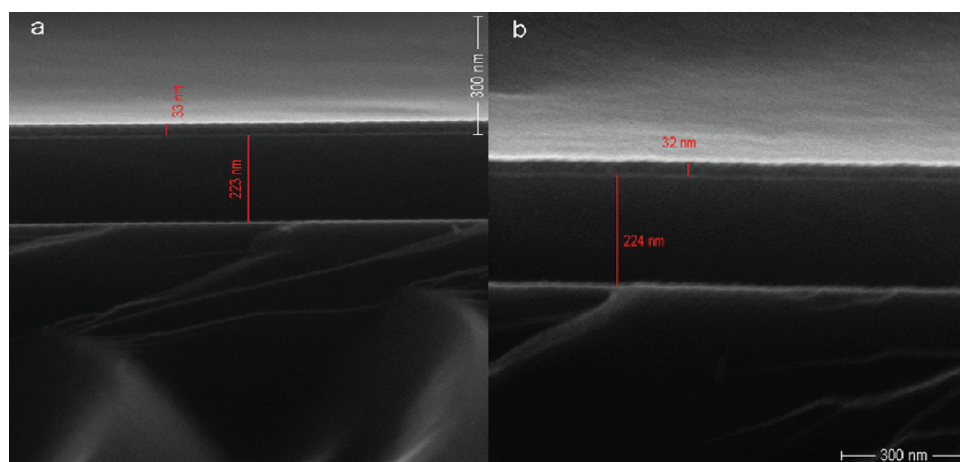


**Figure 11.** Cross-sectional scanning electron microscopy images of tin-rich ITO obtained by coating a toluene solution of **2** on Si-wafers annealed at (a) 250 °C and (b) 350 °C in dry air.

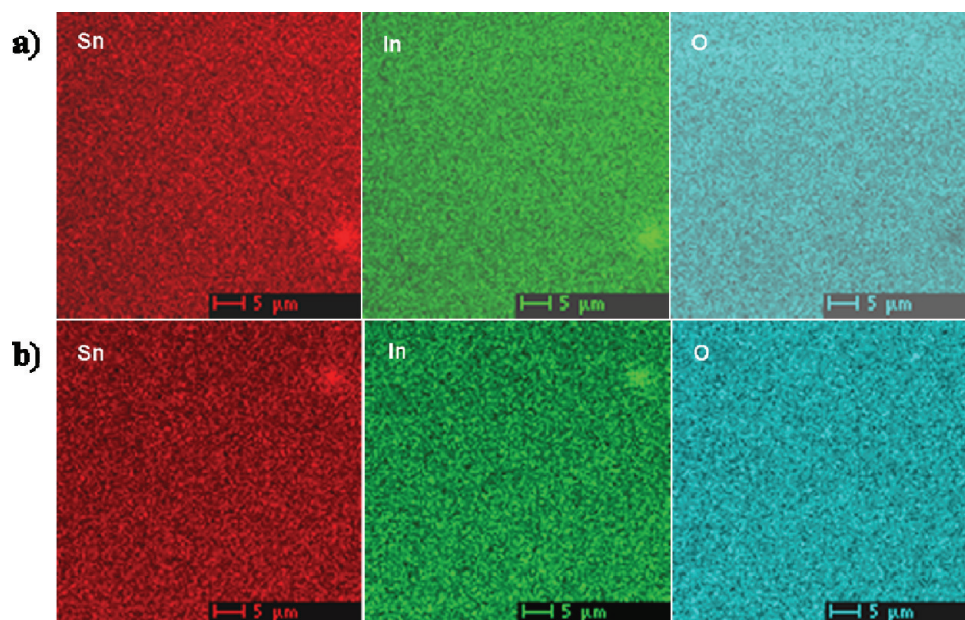


**Figure 12.** X-ray elemental mapping of In and Sn atoms in tin-rich ITO powders recovered from the coating of **2** on Si-wafers annealed at (a) 250 °C and (b) 350 °C obtained from SEM.

synthetic air (20% O<sub>2</sub>, 80% N<sub>2</sub>) with the heating rate of 5 K min<sup>−1</sup> toward the final temperature (700 °C) and subsequent heating time of 2 h at 700 °C.

**Analytical Methods.** <sup>1</sup>H, <sup>13</sup>C, and <sup>119</sup>Sn NMR were recorded on a Bruker spectrometer AV 400. <sup>1</sup>H and <sup>13</sup>C-{<sup>1</sup>H} NMR spectra were referenced to residual solvent signals as internal standard. <sup>119</sup>Sn NMR

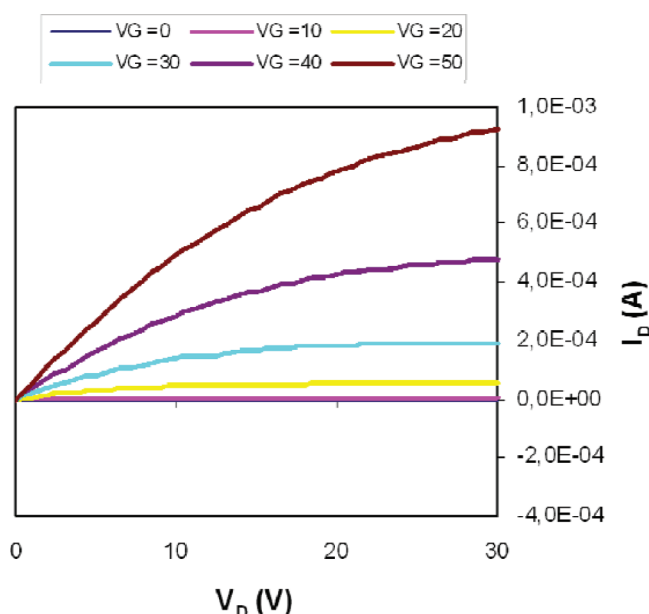


**Figure 13.** Drain current versus drain to source voltage ( $I_D$ – $V_D$ ) output characteristics of the TFT prepared from precursor **2** annealed at 350 °C in air.

**Table 1.** Electrical Performance of Thin Film Transistors Fabricated from Precursor **2**

samples	annealing T (°C)	$\mu_{\text{FET}}$ ( $\text{cm}^2\text{V}^{-1}\text{s}^{-1}$ )	$I_{\text{on}}$ (A)	$I_{\text{on/off}}$ (A)
1	350	$3.7 \times 10^{-1}$	$1 \times 10^{-4}$	$1 \times 10^7$
2	350	$2.3 \times 10^1$	$6 \times 10^5$	$1 \times 10^6$
3	350	$2.10 \times 10^{-1}$	$6 \times 10^{-5}$	$1 \times 10^7$
4	250	$3.9 \times 10^{-2}$	$7 \times 10^{-6}$	$1 \times 10^6$
5	250	$3.18 \times 10^{-2}$	$6 \times 10^{-6}$	$1 \times 10^6$

spectra were referenced to  $\text{SnMe}_4$  as an external standard. Abbreviations: s = singlet; d = doublet; t = triplet; sept = septet; mult = multiplet; br = broad. Solid-state  $^{119}\text{Sn}$  and  $^{13}\text{C}$  magic angle spinning (MAS) measurements were carried out on a Bruker Avance II spectrometer at an external magnetic field of 9.4 T (i.e., a  $^{119}\text{Sn}$  at 149.1 MHz; a  $^{13}\text{C}$  at 101 MHz) using a standard Bruker 4 mm double-resonance H-X MAS probe. The samples were used “as synthesized” and spectra were recorded at a MAS spinning speed of 10 kHz. The isotropic chemical shifts were confirmed by measurements at variable spinning speeds. 5000 transients were recorded for each measurement with a relaxation delay of 100 s. The  $^{119}\text{Sn}$  solid state spectra were referenced externally to  $\text{SnMe}_4$  in  $\text{CDCl}_3$  using solid  $\text{SnO}_2$  as a secondary reference. Infrared spectra were recorded using the KBr pellet technique on a Nicolet Series II Magna-IR Systems 750 FTIR spectrometer in the range 400–4000  $\text{cm}^{-1}$ . Abbreviations: s = strong, m = middle, w = weak, vw = very weak, br = broad. Elemental analysis was performed on a Flash EA 112 Thermo Finnigan elemental analyzer. Melting points were measured on a BSGT melting point apparatus by slowly heating a small quantity of the crystalline compound in a sealed capillary under nitrogen. X-ray powder diffractograms were performed on a Bruker AXS D8 Advance instrument using  $\text{MoK}\alpha$  radiation ( $\lambda = 0.7103 \text{ \AA}$ ) and a position sensitive-detector (PSD) in the  $2\theta$  range from 5 to 90° with 0.015° step. Thermogravimetric analysis (TGA) of the precursors was carried out with a thermogravimetric setup from Rubotherm under synthetic air (20%  $\text{O}_2$ –80%  $\text{N}_2$ ) and with a heating rate of 5 K/min. The EDX samples were measured on carbon coated Cu-TEM grids. Transmission Electron Microscopy (TEM) images were recorded on a Tecnai G<sup>2</sup> 20 S-TWIN (operating at 10 keV) with an energy-dispersive X-ray spectrometer (EDAX, r-TEM SUTW) located at the ZELMI, TU Berlin.

**Single-Crystal X-ray Structure Determination.** Each crystal was mounted on a glass capillary in perfluorinated oil and measured in a cold  $\text{N}_2$  flow. The data of the compounds were collected on an Oxford Diffraction Xcalibur S Sapphire at 150 K ( $\text{Mo-K}\alpha$  radiation),  $\lambda = 0.71073 \text{ \AA}$ . The structures were solved by direct methods and refined on  $F^2$  with the SHELX-97<sup>31</sup> software package. The positions of the H atoms were calculated and considered isotropically according to a riding model. CCDC contain the supplementary crystallographic data for this paper (CCDC 803969 (3); CCDC 803970 (2); CCDC 803971 (4)). The data can be obtained free of charge via [www.ccdc.cam.ac.uk/data\\_request/cif](http://www.ccdc.cam.ac.uk/data_request/cif) or by emailing [data\\_request@ccdc.cam.ac.uk](mailto:data_request@ccdc.cam.ac.uk) or by contacting The Cambridge Crystallographic Data Centre, 12, Union Road, Cambridge CB2 1EZ, UK; fax: +44 1223 336033.

**Synthesis of  $(\text{O}^t\text{Bu})\text{Sn}(\mu_2\text{-O}^t\text{Bu})_2\text{In}(\text{O}^t\text{Bu})_2$  (**1**).** In a typical experiment tin(II) *tert*-butoxide (0.53 g, 2 mmol) was dissolved in 10 mL THF at room temperature and treated with indium *tert*-butoxide (0.69 g, 2 mmol) in 20 mL THF. The reaction mixture was refluxed for an hour. All volatiles were removed *in vacuo* yielding **1** as a colorless amorphous solid in quantitative yield (1.2 g, 2 mmol, 99%). Purification by recrystallization from hexane afforded single crystals suitable for XRD analysis. Melting point: 40 °C.  $^1\text{H}$  NMR (400 MHz,  $\text{C}_6\text{D}_6$ , 25 °C):  $\delta = 1.39$  (s, 36H,  $\text{C}(\text{CH}_3)_3$ ), 1.49 (br. s, 9H,  $\text{C}(\text{CH}_3)_3$ ), 1.57 ppm (br. s, 45H,  $\text{C}(\text{CH}_3)_3$ ).  $^{13}\text{C}$  NMR (101 MHz,  $\text{C}_6\text{D}_6$ , 25 °C):  $\delta = 34.8$  ( $\text{C}(\text{CH}_3)_3$ ), 35.4 (br.  $\text{C}(\text{CH}_3)_3$ ), 72.2 (br.  $\text{C}(\text{CH}_3)_3$ ), 74.5 ppm ( $\text{C}(\text{CH}_3)_3$ ).  $^{119}\text{Sn}$ -NMR (149 MHz,  $\text{C}_6\text{D}_6$ , 25 °C):  $\delta = -201$  ppm IR (KBr):  $\nu = 2964$  (s), 2923 (m), 2899 (m), 2864 (m), 1470 (m), 1385 (s), 1358 (s), 1240 (m), 1189 (s), 962 (s), 902 (s), 829 (w), 758 (m), 662 (w), 595 (s), 468 (m) EI-MS (70 eV):  $m/z$  (%): 527.21 (100) [ $\text{M}^+$ -O<sup>t</sup>Bu] Elemental anal. Calcd for  $\text{C}_{20}\text{H}_{45}\text{InO}_5\text{Sn}$  (%): C, 36.00; H, 6.80. Found: C, 36.84; H, 6.87.

**Synthesis of  $(^t\text{BuO})\text{Sn}(\mu_2\text{-O}^t\text{Bu})_2\text{In}(\text{N}(\text{SiMe}_3)_2)_2$  (**2**).** In a typical experiment, tin(II) hexamethyl-disilazide (0.88 g, 2 mmol) was dissolved in 10 mL of THF at room temperature and treated with indium *tert*-butoxide (0.67 g, 2 mmol) in 20 mL of THF. The reaction mixture was refluxed for an hour, and then all volatiles were removed *in vacuo* yielding **2** as a colorless solid in quantitative yield (1.55 g, 2 mmol, 99%). Recrystallization from hexane yielded single crystals suitable for XRD analysis. Melting point: 45 °C.  $^1\text{H}$  NMR (400 MHz,  $\text{C}_6\text{D}_6$ , 25 °C):  $\delta = 0.39$  (s, 18H,  $\text{N}[\text{Si}(\text{CH}_3)_3]$ ), 0.44 (s, 18H,  $\text{N}[\text{Si}(\text{CH}_3)_3]$ ), 1.35 (s, 9H,  $\text{C}(\text{CH}_3)_3$ ), 1.35 ppm (br. s, 18H,  $\text{C}(\text{CH}_3)_3$ ).  $^{13}\text{C}$  NMR (101 MHz,  $\text{C}_6\text{D}_6$ , 25 °C):  $\delta = 7.23$  ( $\text{N}[\text{Si}(\text{CH}_3)_3]$ ), 34.4 (br.  $\text{C}(\text{CH}_3)_3$ ), 35.4 ( $\text{C}(\text{CH}_3)_3$ ), 71.9 ( $\text{C}(\text{CH}_3)_3$ ), 76.0 ppm (br.  $\text{C}(\text{CH}_3)_3$ ).  $^{119}\text{Sn}$ -NMR (149 MHz,  $\text{C}_6\text{D}_6$ , 25 °C):  $\delta = -190$  ppm.  $^{29}\text{Si}$ -[INEPT]-NMR (79.4 MHz,  $\text{C}_6\text{D}_6$ , 25 °C):  $\delta = 2.17$ , 2.37 ppm IR (KBr):  $\nu = 2962$  (s), 2908 (m), 2861 (m), 1457 (w), 1363 (m), 1248 (m), 1192 (m), 1172 (m), 955 (w), 913 (s), 897 (m), 885 (m), 865 (m), 831 (m), 792 (w), 754 (m), 666 (m), 617 (w), 580 (m), 563 (m), 461 (w) EI-MS (70 eV):  $m/z$  (%): 758.96 (100) [ $\text{M}^+$ -Me] Elemental anal. Calcd for  $\text{C}_{24}\text{H}_{63}\text{InN}_2\text{O}_3\text{Si}_4\text{Sn}$  (%): C, 45.46; H, 6.99. Found: C, 46.84; H, 6.94.

**Synthesis of  $\text{In}_3\text{Sn}_4(\text{O}^t\text{Bu})_6\text{Cl}_7\text{O}_2$  (**3**).** In a typical experiment, indium(III) chloride (0.66 g, 3 mmol) was dissolved in 10 mL THF at room temperature and treated with tin(II) *tert*-butoxide (1.32 g, 5 mmol) in 20 mL THF. The reaction mixture was allowed to stir overnight at room temperature. All volatiles were removed *in vacuo* and remaining colorless solid was recrystallized from THF yielding single crystals suitable for XRD analysis (0.61 g, 0.4 mmol, 40%). Melting point: 240 °C.  $^1\text{H}$  NMR (400 MHz,  $\text{C}_6\text{D}_6$ , 25 °C):  $\delta = 1.49$  ppm (br., 54H,  $\text{C}(\text{CH}_3)_3$ ).  $^{13}\text{C}$  NMR (101 MHz,  $\text{C}_6\text{D}_6$ , 25 °C):  $\delta = 34.78$  ( $\text{C}(\text{CH}_3)_3$ ), 76.6 ppm ( $\text{C}(\text{CH}_3)_3$ ). Solid-state  $^{13}\text{C}\{^1\text{H}\}$ -NMR (101 MHz,  $\text{C}_6\text{D}_6$ , 25 °C, CP/MAS):  $\delta = 32.23$  (br.,  $\text{C}(\text{CH}_3)_3$ ), 33.08 (br.,  $\text{C}(\text{CH}_3)_3$ ), 33.59 (br.,  $\text{C}(\text{CH}_3)_3$ ), 76.96 (br.,  $\text{C}(\text{CH}_3)_3$ ), 80.73 (br.,  $\text{C}(\text{CH}_3)_3$ ), 82.1 (br.,  $\text{C}(\text{CH}_3)_3$ ).  $^{119}\text{Sn}$ -NMR (149 MHz,  $\text{C}_6\text{D}_6$ , 25 °C):  $\delta = -300$  ppm. Solid-state  $^{119}\text{Sn}\{^1\text{H}\}$ -NMR (149 MHz,  $\text{SnMe}_4$ , 25 °C, CP/MAS):  $\delta = -282$  ppm; IR (KBr):  $\nu = 2977$  (s), 2956 (s), 2925 (s), 2896 (s), 2863 (s), 1469 (m), 1391 (m), 1364 (s), 1240 (m), 1174 (s), 1031 (m), 919 (s), 900 (m), 871 (m), 758 (m), 674 (w), 580 (s), 555 (m), 496 (w), 465 (s). Elemental anal. Calcd for  $\text{C}_{24}\text{H}_{54}\text{Cl}_7\text{In}_3\text{O}_8\text{Sn}_4$  (%): C, 18.74; H, 3.54. Found: C, 18.94; H, 3.49



### Synthesis of $\text{In}_3\text{Sn}_4(\text{O}^t\text{Bu})_6\text{Cl}_2\text{O}_2 \cdot \text{In}_3\text{Sn}_4(\text{O}^t\text{Bu})_7\text{Cl}_6\text{O}_2 \cdot \text{C}_6\text{H}_5\text{CH}_3$ (**4**).

In a typical experiment, indium(III) chloride (0.63 g, 2.86 mmol) was dissolved in 20 mL of THF at room temperature and treated with tin(II) *tert*-butoxide (1.32 g, 5 mmol) in 10 mL of THF. The reaction mixture was allowed to stir overnight at room temperature. All volatiles were removed in vacuo and remaining colorless solid was redissolved in toluene. The white precipitate of  $\text{SnCl}_2$  was filtered off, the filtrate concentrated and kept at  $-20^\circ\text{C}$  overnight, yielding **4** in form of single crystals suitable for XRD analysis (1.07 g, 0.7 mmol, 70%). Melting point:  $210^\circ\text{C}$ .  $^1\text{H}$  NMR (400 MHz,  $\text{C}_6\text{D}_6$ ,  $25^\circ\text{C}$ ):  $\delta$  = 1.30 (s, br., 18H,  $\text{C}(\text{CH}_3)_3$ ), 1.55 (s, 18H,  $\text{C}(\text{CH}_3)_3$ ), 1.56 (s, 27H,  $\text{C}(\text{CH}_3)_3$ ), 1.66 ppm (s, 54H,  $\text{C}(\text{CH}_3)_3$ ), 2.1 (s, 3H,  $\text{CH}_3\text{C}_6\text{H}_5$ ) 7.01 ppm (m, 5H,  $\text{CH}_3\text{C}_6\text{H}_5$ ).  $^{13}\text{C}$  NMR (101 MHz,  $\text{C}_6\text{D}_6$ ,  $25^\circ\text{C}$ ):  $\delta$  = 21.38 ( $\text{CH}_3\text{C}_6\text{H}_5$ ), 30.97 (br.,  $\text{C}(\text{CH}_3)_3$ ), 32.88 ( $\text{C}(\text{CH}_3)_3$ ), 33.85 ( $\text{C}(\text{CH}_3)_3$ ), 34.14 (br.,  $\text{C}(\text{CH}_3)_3$ ), 75.87 ( $\text{C}(\text{CH}_3)_3$ ), 80.19 ppm ( $\text{C}(\text{CH}_3)_3$ ), 125.64 ( $\text{CH}_3\text{C}_6\text{H}_5$ ), 128.51 ( $\text{CH}_3\text{C}_6\text{H}_5$ ), 129.28 ( $\text{CH}_3\text{C}_6\text{H}_5$ ), 137.84 ppm ( $\text{CH}_3\text{C}_6\text{H}_5$ ). Solid-state  $\text{C}\{^1\text{H}\}$ -NMR (101 MHz,  $\text{C}_6\text{D}_6$ ,  $25^\circ\text{C}$ , CP/MAS):  $\delta$  = 21.9 ( $\text{CH}_3\text{C}_6\text{H}_5$ ), 31.6 (br.,  $\text{C}(\text{CH}_3)_3$ ), 32.8 (br.,  $\text{C}(\text{CH}_3)_3$ ), 33.5 (br.,  $\text{C}(\text{CH}_3)_3$ ), 34.2 (br.,  $\text{C}(\text{CH}_3)_3$ ), 75.5 (br.,  $\text{C}(\text{CH}_3)_3$ ), 78.4 (br.,  $\text{C}(\text{CH}_3)_3$ ), 80.0 (br.,  $\text{C}(\text{CH}_3)_3$ ), 124.7 ( $\text{CH}_3\text{C}_6\text{H}_5$ ), 127.4 ( $\text{CH}_3\text{C}_6\text{H}_5$ ), 127.9 ( $\text{CH}_3\text{C}_6\text{H}_5$ ), 136.7 ppm ( $\text{CH}_3\text{C}_6\text{H}_5$ ).  $^{119}\text{Sn}$ -NMR (149 MHz,  $\text{C}_6\text{D}_6$ ,  $25^\circ\text{C}$ ):  $\delta$  =  $-445$  ppm. Solid-state  $^{119}\text{Sn}\{^1\text{H}\}$ -NMR (149 MHz,  $\text{SnMe}_4$ ,  $25^\circ\text{C}$ , CP/MAS):  $\delta$  =  $-475$  ppm IR (KBr):  $\nu$  = 2961 (s), 2921 (s), 2861 (s), 1471 (m), 1390 (m), 1367 (m), 1239 (m), 1169 (s), 1028 (w), 982 (w), 888 (s), 757 (m), 727 (w), 693 (w), 582 (w), 499 (w), 477 (w), 447 (w) Elemental anal. Calcd for  $\text{C}_{33}\text{H}_{66.5}\text{Cl}_{6.5}\text{In}_3\text{O}_{8.5}\text{Sn}_4$  (%): C, 24.01; H, 3.57. Found: C, 23.69; H, 3.58

## ■ ASSOCIATED CONTENT

### Supporting Information

Additional NMR spectroscopic data for compounds **1–4**, details on the single-crystal XRD characterization of precursors **2**, **3**, and **4**, as well as PXRD, EDX spectra, and FET characteristics of the degradation product of **1**. This material is available free of charge via the Internet at <http://pubs.acs.org>

## ■ AUTHOR INFORMATION

### Corresponding Author

\*Phone: +49 (0)30-314-22265. Fax: +49 (0)30-314-29732. E-mail: [matthias.driess@mailbox.tu-berlin.de](mailto:matthias.driess@mailbox.tu-berlin.de).

### Notes

The authors declare no competing financial interest.

## ■ ACKNOWLEDGMENTS

We thank the Evonik Industries-Degussa (Marl) Science-to-Business Center Nanotronics (Marl) for cooperation, the Cluster of Excellence “UniCat: Unifying Concepts in Catalysis” (sponsored by the Deutsche Forschungsgemeinschaft and administrated by the Technische Universität Berlin) for financial support. We also thank the ZELMI-team (Zentrales Laboratorium für Elektronenmikroskopie, TU-Berlin), the research group of Prof. Dr. Helmut Schubert, in particular Dr. Oliver Goerke (TU-Berlin) for ICP-OES, Dr. Elisabeth Irran for the X-ray structure elucidation, Dr. J.-D. Epping, and Dr. Heinz-Jürgen Kroth, for NMR measurements. This work is in memory of Professor Helmut Schubert.

## ■ REFERENCES

- (1) (a) Ginley, D. S.; Bright, C. *MRS Bull.* **2000**, 25, 15. (b) Minami, T. *Semicond. Sci. Technol.* **2005**, 20, S35.
- (2) Lewis, B. G.; Paine, D. C. *MRS Bull.* **2000**, 25, 22.
- (3) Ziegler, J. P.; Howard, B. M. *Electrochem. Soc. Interface* **1994**, 3, 27.
- (4) (a) Gazotti, W. A.; Casalbore-Miceli, G.; Geri, A.; Berlin, A.; Paoli, M. a. D. *Adv. Mater.* **1988**, 10, 1522. (b) Pichot, F.; Ferrere, S.; Pitts, R. J.; Gregg, B. A. *J. Electrochem. Soc.* **1999**, 146, 3949.
- (c) Granqvist, C. G.; Hultaker, A. *Thin Solid Films* **2002**, 411, 1.
- (d) Xu, C. Y.; Liu, L.; Legenski, S. E.; Ning, D.; Taya, M. *J. Mater. Res.* **2004**, 19, 2072.
- (5) (a) Kobayashi, H.; Ishida, T.; Nakato, Y.; Tsubomura, Y. *J. Appl. Phys.* **1991**, 69, 1736. (b) Martinez, M. A.; Herrero, J.; Gutierrez, M. T. *Thin Solid Films* **1995**, 269, 80.
- (6) (a) Forleo, A.; Francioso, L.; Epifani, M.; Capone, S.; Taurino, A. M.; Siciliano, P. *Thin Solid Films* **2005**, 490, 68. (b) Vaishnav, V. S.; Patel, P. D.; Patel, N. G. *Thin Solid Films* **2005**, 487, 277.
- (7) Patel, N. G.; Patel, P. D.; Vaishnav, V. S. *Sens. Actuators B* **2003**, 96, 180.
- (8) (a) Hamberg, I.; Granqvist, C. G. *J. Appl. Phys.* **1986**, 60, R123. (b) Gordon, R. G. *MRS Bull.* **2000**, 25, S2.
- (9) Canhola, P.; Martins, N.; Raniero, L.; Pereira, S.; Fortunato, E.; Ferreira, I.; Martins, R. *Thin Solid Films* **2005**, 487, 271.
- (10) Ma, J.; Zhang, D.; Zhao, J.; Tan, C.; Yang, T.; Ma, H. *Appl. Surf. Sci.* **1999**, 151, 239.
- (11) Chopra, K. L.; Major, S.; Pandya, D. K. *Thin Solid Films* **1983**, 102, 1.
- (12) (a) Zheng, J. P.; Kwok, H. S. *Appl. Phys. Lett.* **1993**, 63, 1. (b) Wan, Q.; Feng, P.; Wang, T. H. *Appl. Phys. Lett.* **2006**, 89, 123102.
- (13) (a) Maruyama, T.; Fukui, K. *J. Appl. Phys.* **1991**, 70, 3848. (b) Ni, J.; Yan, H.; Wang, A.; Yang, Y.; Stern, C. L.; Metz, A. W.; Jin, S.; Wang, L.; Marks, T. J.; Ireland, J. R.; Kanneur, C. R. *J. Am. Chem. Soc.* **2005**, 127, 5613.
- (14) (a) Kundu, S.; Biswas, P. K. *Chem. Phys. Lett.* **2005**, 414, 107. (b) Epifani, M.; Diaz, R.; Arbiol, J.; Siciliano, P.; Morante, J. R. *Chem. Mater.* **2006**, 18, 840.
- (15) (a) Goebert, C.; Nonninger, R.; Aegerter, M. A.; Schmidt, H. *Thin Solid Films* **1999**, 351, 79. (b) Al-Dahoudi, N.; Aegerter, M. A. *J. Sol-Gel Sci. Technol.* **2003**, 26, 693. (c) Ederth, J.; Heszler, P.; Hultaker, A.; Niklasson, G. A.; Granqvist, C. G. *Thin Solid Films* **2003**, 445, 199. (d) J. Ederth, J.; Johnsson, P.; Niklasson, G. A.; Hoel, A.; Hultaker, A.; Heszler, P.; Granqvist, C. G.; Doorn, A. R. V.; Jongerius, M. J.; Burgard, D. *Phys. Rev. B* **2003**, 68, 155410/1. (e) Niederberger, M.; Garnweitner, G.; Pinna, N.; Prog, G. *Solid State Chem. Mater.* **2005**, 33, 59. (f) Ba, J.; Rohlfing, D. F.; Feldhoff, A.; Brezesinski, T.; Djerdj, L.; Wark, M.; Niederberger, M. *Chem. Mater.* **2006**, 18, 2848. (g) Kanehara, M.; Koike, H.; Yoshinaga, T.; Teranishi, T. *J. Am. Chem. Soc.* **2009**, 131, 17736.
- (16) Frank, G.; Köstlin, H. *Appl. Phys. A: Mater. Sci. Process.* **1982**, 27, 197.
- (17) (a) Aksu, Y.; Driess, M. *Angew. Chem., Int. Ed.* **2009**, 48 (42), 7778. (b) Aksu, Y.; Frasca, S.; Wollenberger, U.; Driess, M.; Thomas, A. *Chem. Mater.* **2011**, 23 (7), 1798. (c) Heitz, S.; Aksu, Y.; Merschjann, C.; Driess, M. *Chem. Mater.* **2010**, 22 (4), 1376. (d) Heitz, S.; Epping, J.-D.; Aksu, Y.; Driess, M. *Chem. Mater.* **2010**, 22 (16), 4563. (e) Heitz, S.; Aksu, Y.; Merschjann, C.; Driess, M. *Chem.—Eur. J.* **2011**, 17 (14), 3904.
- (18) Kumar, N.; Parajuli, O.; Feng, M.; Xu, J.; Hahm, J. *Appl. Phys. Lett.* **2010**, 96, 053705.
- (19) Veith, M. *J. Chem. Soc., Dalton Trans.* **2002**, 2405.
- (20) (a) Polarz, S.; Orlov, A. V.; Berg, M. W. E. v. d.; Driess, M. *Angew. Chem., Int. Ed.* **2005**, 44, 7892. (b) Jana, S.; Aksu, Y.; Driess, M. *Dalton Trans.* **2009**, 9, 1516. (c) Arndt, S.; Aksu, Y.; Driess, M.; Schomaecker, R. *Catal. Lett.* **2009**, 131 (1–2), 258. (d) Ma, J.-G.; Aksu, Y.; Gregoriades, L. J.; Sauer, J.; Driess, M. *Dalton Trans.* **2010**, 39 (1), 103. (e) Tsaroucha, M.; Aksu, Y.; Irran, E.; Driess, M. *Chem. Mater.* **2011**, 23 (9), 2428. (f) Samedov, K.; Aksu, Y.; Driess, M. *Chem. Eur. J.* **2012**, DOI 10.1002/chem.201103594.
- (21) Veith, M.; Hill, S.; Huch, V. Z. *Anorg. Allg. Chem.* **2001**, 627, 1495.
- (22) Bradley, D. C.; Mehrotra, R. C.; Gaur, P. D. *Metal Alkoxides*; Academic Press: London, 1978.
- (23) Veith, M.; Mathur, S.; Mathur, C. *Polyhedron* **1998**, 17, 1005.
- (24) (a) Bradley, D. C.; Chudzynska, H.; Frigo, D. M.; Hursthouse, M. B.; Mazid, M. A. *J. Chem. Soc., Chem. Commun.* **1988**, 1258. (b) Bradley, D. C.; Frigo, D. M.; Hursthouse, M. B.; Hussain, B.

- Organometallics* **1988**, 7, 1112–1115. (c) Zybill, C.; Müller, G. Z. *Naturforsch.* **1988**, 43b, 45. (d) Veith, M.; Hill, S.; Huch, V. *Eur. J. Inorg. Chem.* **1999**, 1342.
- (25) Kim, J.; Bott, S. G.; Hoffman, D. M. *Inorg. Chem.* **1998**, 37, 3835.
- (26) Veith, M.; Recktenwald, O. J. *Organomet. Chem.* **1984**, 264, 19.
- (27) Veith, M.; Kafer, D.; Koch, J.; May, P.; Stahl, L.; Huch, V. *Chem. Ber.* **1992**, 125, 1033.
- (28) Quaas, M.; Eggs, C.; Wulff, H. *Thin Solid Films* **1998**, 332, 277.
- (29) Veith, M.; Töllner, F. J. *Organomet. Chem.* **1983**, 246, 219.
- (30) Herve, A.; Rodriguez, A. L.; Fouquet, E. J. *Org. Chem.* **2005**, 70, 1953.
- (31) Sheldrick, G. M. *SHELX-97, Program for Crystal Structure Refinement*; University of Göttingen: Göttingen, Germany, 1997.